Electronic Supplementary Material (ESI) for Nanoscale Horizons.
This journal is © The Royal Society of Chemistry 2023

Supporting Information

Transition Metal Single Atoms Optimizing g-C_3N_4 for Highly Selective Electrosynthesis of H_2O_2 under Neutral Electrolytes

Hongcen Yang,[#] Fei Ma,[#] Niandi Lu, Shuhao Tian, Guo Liu, Ying Wang, Zhixia Wang, Di Wang, Kun Tao, Hong Zhang,[*] Shanglong Peng.[*]

School of Physical Science and Technology, School of Materials and Energy, Electron Microscopy Centre of Lanzhou University, Lanzhou University, Lanzhou 730000, China

*Corresponding authors. E-mail: pengshl@lzu.edu.cn (S.L. Peng).

Table of Contents

13. **Figure S12.** (a) ORR disk current density together with the ring currents at a fixed potential of 1.20 V vs. RHE, (b) H_2O_2 selectivity (H_2O_2 %), (c) the calculated electron transfer number (n) and (d) the faradaic efficiency (FE%) of CNNS, $Ni_{0.05}$ SA/CNNS, $Ni_{0.10}$ SA/CNNS and $Ni_{0.20}$ SA/CNNS in 0.1 M PBS.
14. **Figure S13.** (a) The calculated electron transfer number (n) and (b) the faradaic efficiency (FE%) of CNNS, $Ni_{0.10}$ SA/CNNS and other TM SA/CNNS in 0.1 M PBS.
15. **Figure S14.** CV curves of (a) CNNS, (b) $Ni_{0.10}$ SA/CNNS, (c) $Mn_{0.10}$ SA/CNNS, (d) $Zn_{0.10}$ SA/CNNS, (e) $Cu_{0.10}$ SA/CNNS, (f) $Fe_{0.10}$ SA/CNNS and (g) $Co_{0.10}$ SA/CNNS measured in 0.1 M PBS at different scan rates (10, 20, 40, 60, and 80 mV s^{-1}).
16. **Figure S15.** Selectivity and the calculated electron transfer number (n) corresponding to stability measurements of $Ni_{0.10}$ SA/CNNS at a fixed disk potential of 0.3 V vs. RHE.
17. **Figure S16.** The comparison of (a) current densities, (b) selectivity, (c) the calculated electron transfer number (n) and (d) the faradaic efficiency (FE%) of the same $Ni_{0.10}$ SA/CNNS ink before and after 68 days
18. **Figure S17.** (a) The absorbance value of $Ce(SO_4)_2$ with different concentrations. (b) The linear relationship between the concentration of $Ce(SO_4)_2$ and the absorbance.
19. **Figure S18.** (a) I-t curves of CNNS in O_2-saturted 0.1 M PBS at different potentials. (b) The absorbance value of $Ce(SO_4)_2$ after reacting with H_2O_2 that produced by CNNS at different potentials.
20. **Figure S19.** (a) I-t curves of $Ni_{0.10}$ SA/CNNS in O_2-saturted 0.1 M PBS at different potentials. (b) The absorbance value of $Ce(SO_4)_2$ after reacting with H_2O_2 that produced by $Ni_{0.10}$ SA/CNNS at different potentials.
21. **Figure S20.** (a) I-t curves of $Mn_{0.10}$ SA/CNNS in O_2-saturted 0.1 M PBS at different potentials. (b) The absorbance value of $Ce(SO_4)_2$ after reacting with H_2O_2 that produced by $Mn_{0.10}$ SA/CNNS at different potentials.

22. **Figure S21.** (a) I-t curves of $Zn_{0.10}$ SA/CNNS in O_2-saturted 0.1 M PBS at different potentials. (b) The absorbance value of $Ce(SO_4)_2$ after reacting with H_2O_2 that produced by $Zn_{0.10}$ SA/CNNS at different potentials.
23. **Figure S22.** (a) I-t curves of $Cu_{0.10}$ SA/CNNS in O_2-saturted 0.1 M PBS at different potentials. (b) The absorbance value of $Ce(SO_4)_2$ after reacting with H_2O_2 that produced by $Cu_{0.10}$ SA/CNNS at different potentials.
24. **Figure S23.** (a) I-t curves of $Fe_{0.10}$ SA/CNNS in O_2-saturted 0.1 M PBS at different potentials. (b) The absorbance value of $Ce(SO_4)_2$ after reacting with H_2O_2 that produced by $Fe_{0.10}$ SA/CNNS at different potentials.
25. **Figure S24.** (a) I-t curves of $Co_{0.10}$ SA/CNNS in O_2-saturted 0.1 M PBS at different potentials. (b) The absorbance value of $Ce(SO_4)_2$ after reacting with H_2O_2 that produced by $Co_{0.10}$ SA/CNNS at different potentials.
26. **Figure S25.** (a) and (b) The absorbance value of $Ce(SO_4)_2$ after reacting with H_2O_2 that produced by $Ni_{0.10}$ SA/CNNS at different times.
27. **Figure S26.** The rate of H_2O_2 of $Ni_{0.10}$ SA/CNNS at different times.
28. **Table S1**. The crystallite size of CNNS, $Ni_{0.10}$ SA/CNNS and other TM SA/CNNS, which is calculated by Debye-Scherrer equation based on the XRD patterns.
29. **Table S2.** EXAFS fitting parameters at the Ni k-edge for various samples (S_0^2=0.778)
30. **Table S3**. The atomic percentages of carbon species (N-C=N, C-O, C-C/C=C) in CN, $Ni_{0.10}$ SA/CNNS, $Mn_{0.10}$ SA/CNNS, $Zn_{0.10}$ SA/CNNS, $Cu_{0.10}$ SA/CNNS, $Fe_{0.10}$ SA/CNNS and $Co_{0.10}$ SA/CNNS.
31. **Table S4** The comparisons of different electrocatalysts towards $2e^-$ ORR at different pH.

Supplemental Text S1

1 Experimental sections

1.1 Materials synthesis

1.1.1 Chemical reagents and materials

All these chemical reagents and materials were all purchased from Sinopharm. Chemical Reagent Co., Ltd. And they were analytical grade and used without any further purification.

1.1.2 Preparation process of g-C_3N_4 nanosheets

A certain amount of urea and dicyandiamide (DCDA) (mass ratio of urea and dicyandiamide is 7 : 3) were solved in 50 ml deionized water, the liquid was frozen with liquid nitrogen and dried by vacuum freeze-drying, thereby obtaining a uniformly mixed precursor. The obtained precursor was added to a crucible and heated to 550 °C in a muffle furnace at 2.5 °C min^{-1}, then maintained for 4 h to obtain the initial g-C_3N_4. The initial g-C_3N_4 was further heat-treated in 10% Ar/H_2 at 500°C and 5°C min^{-1} for 2 h. Finally, g-C_3N_4 nanosheets (CNNS) were obtained.

1.1.3 Preparation of Ni single atom/g-C_3N_4 nanosheets

Firstly, 7 g urea, 3 g dicyandiamide and a certain amount of $NiCl_2 \cdot 6H_2O$ (0.05, 0.1, 0.2 mmoL) were also solved in 50 ml deionized water, the liquid was frozen with liquid nitrogen and dried by vacuum freeze-drying, thereby obtaining a uniformly mixed precursor. The precursor was also filled into a crucible and heated to 550 °C in a muffle furnace at 2.5 °C min^{-1}, then maintained for 4 h to obtain the initial Ni single atom/g-C_3N_4 nanocomposites. The obtained initial Ni single atom/g-C_3N_4 nanocomposites were further heat-treated in 10% Ar/H_2 at 500°C

and 5°C min^{-1} for 2 h. Thereby, Ni single atom/g-C_3N_4 nanosheets (Ni SA/CNNS) were obtained and were named as $Ni_{0.05}$ SA/CNNS, $Ni_{0.10}$ SA/CNNS, $Ni_{0.20}$ SA/CNNS, respectively.

1.1.4 Preparation of other transition metals single atoms/g-C_3N_4 nanosheets

Similar to the preparation method of Ni SA/CNNS shown in section 2.1.3, other transition metal chlorides (0.10 mmoL $MCl_x \cdot ZH_yO$, M=Mn, Fe, Co, Cu, Zn) were used instead of $NiCl_2 \cdot 6H_2O$ as the metal source to prepare other transition metals single atom/g-C_3N_4 nanosheets (TM SA/CNNS), which were named as $Mn_{0.10}$ SA/CNNS, $Fe_{0.10}$ SA/CNNS, $Co_{0.10}$ SA/CNNS, $Cu_{0.10}$ SA/CNNS, $Zn_{0.10}$ SA/CNNS, respectively.

1.2 Characterization methods

X-ray diffraction data (XRD) of electrocatalysts was obtained by X-ray diffractometer D/MAX-2400 using Cu Kα radiation (λ = 1.5418 Å). The size, morphology and compositions of pure CNNS and TM SA/CNNS were confirmed by field emission scanning electron microscope (Apero S), tecnai F30 field emission transmission electron microscope and Spectra 300 high-angle annular dark field-scanning transmission election microscope. X-ray photoelectron spectroscopy (XPS) of pure CNNS and TM SA/CNNS was performed using Kratos AXIS Ultra DLD X-ray photoelectron spectrometer using a Mg Kα source (15 kV, 10 mA) and the C1s peak at 284.6 eV as an internal standard. The rotating ring-disk electrode (RRDE) assembly (PGSTAT-302N, USA) consists of a glassy carbon rotation disk electrode (disk area: 0.2475 cm^2) and a Pt ring (ring area: 0.1866 cm^2), with a collection efficiency (N) of 37%. UV-Vis spectrums were measured via PerkinElmer LAMBDA 950 UV Spectrophotometer.

Data reduction, data analysis, and EXAFS fitting were performed according to the standard procedures using the ATHENA and ARTEMIS program intergrated within the Demeter packages. The energy calibration of the sample was conducted through a standard Ni foil, which

as a reference was simultaneously measured. For EXAFS modeling, The *k3*-weighted EXAFS spectra were obtained via subtracting the post-edge background from the overall absorption, normalization with respect to the edge-jump step, and Fourier transformation to real (*R*) space using a Hanning windows (*dk* = 1.0 Å) ranging from 3.0-12.5 $Å^{-1}$. EXAFS of the Ni foil is fitted and the obtained amplitude reduction factor $S0^2$ value (0.778) was set in the EXAFS analysis to determine the coordination numbers (*CNs*) in the Ni -N/C scattering path in sample.

1.3 Electrochemical measurements

Electrocatalytic performance tests are carried out with a three-electrode system controlled by a CHI 760E electrochemical station. A graphite rod, Hg/HgO electrode and rotating ring-disk electrode were used as the counter electrode, reference electrode and working electrode, respectively. Preparation of inks: 5 mg of catalyst and 5 mg of carbon were sonicated and dispersed into isopropanol (2000 μL) containing 40 μL of 5 wt% Nafion solutions. Then 10 μL inks were dropped onto the polished RRDE and the loading of the catalysts on the electrode was 0.1 $mg \cdot cm^{-2}$. All the measurements were carried out in O_2-saturated neutral aqueous solution (0.10 M PBS (phosphate buffer solution)). The rotating speed of RRDE was 1600 rpm. The ring electrode was set at a constant potential of 1.20 V vs. RHE (reversible hydrogen electrode) to detect the generated H_2O_2. All the recorded potentials were corrected to the RHE by calibration. All the electrocatalysts were stabilized in advance by cyclic voltammetry (CV) with a scan rate of 10 mV s^{-1} and then linear sweep voltammetry (LSV) was conducted at a scan rate of 5 mV s^{-1}. The selectivity of H_2O_2 (the percentage of H_2O_2 in the product released during oxygen reduction reaction), the number of electrons transferred (n) and the faradaic efficiency (FE %) were obtained from the equations:

The selectivity of H_2O_2 (%) = $200 \times I_r/(N \times |I_d| + I_r)$

$n = 4\times|I_d|/(|I_d|+I_r/N)$

$FE\ (\%) = 100\times(I_r/N)/|I_d|$

Where I_r is the ring current (μA), I_d is the absolute value of the disk current (μA).

Tafel slopes were calculated from the Tafel equation:

$\eta = b\times\log(j/j_0)$

Where η is the overpotential, b is the Tafel slope, j is the current density, and j_0 is the exchange current density.

H_2O_2 production was conducted by chronoamperometry with the applied potential of 0.1, 0.2, and 0.3 V vs. RHE at 25 °C in H-Cell. The catalysts were dripped on carbon paper (1×1 cm^2), and the areal loading area was 1 $mg\cdot cm^{-2}$. The cerium sulfate ($Ce(SO_4)_2$) was used in this experiment to calculate the concentration of H_2O_2 owing to the reaction:

$2Ce^{4+}+H_2O_2\rightarrow 2Ce^{3+}+2H^{+}+O_2$

The yellow solutions of Ce^{4+} react with H_2O_2 and generate the colorless Ce^{3+}. First of all, 1 mM $Ce(SO_4)_2$ was obtained by dispersing 33.2 mg $Ce(SO_4)_2$ in 100 mL 0.5 M H_2SO_4. Then ultraviolet-visible spectrum (UV-vis) technology was used to obtain the calibration curve between the concentration of Ce^{4+} and absorbance. The linear relationship between the concentration (C) of $Ce(SO_4)_2$ and the absorbance (A) was: A = 2.4685C (R = 0.9992). According to the linear equation, the concentration of H_2O_2 generated from the reaction can be easily known. The concentration of H_2O_2 can be calculated as following:

$C(H_2O_2) = 1/2\times(C_0(Ce^{4+})-C(Ce^{4+}))$

Where $C(H_2O_2)$ is the concentration of H_2O_2, $C_0(Ce^{4+})$ is the initial concentration of $Ce(SO_4)_2$, $C(Ce^{4+})$ is the concentration of $Ce(SO_4)_2$ after reaction with H_2O_2.

1.4 Methods and Models

Spin-polarized density functional theory (DFT) method was performed with the Vienna ab initio Simulation Package (VASP).[1] The electronic exchange-correlation energy was modelled using the Perdew-Burke-Ernzerhof (PBE) functional within the generalised gradient approximation (GGA).[2] The projector augmented wave (PAW) method was used to describe the ionic cores.[3] For the plane-wave expansion, a 500 eV kinetic energy cut-off was used. A Monkhorst-Pack 5 × 5 × 1 k-point grid was used to sample the Brillouin zone. The convergence value of energy in DFT calculation was set to be 10^{-5} eV.[3] The convergence value of force in geometric optimization is set to be 0.01 eV/Å. A Gaussian smearing of 0.2 eV was applied during the geometry optimisation and for the total energy computations. To better describe the dispersion interaction within adsorption systems, vdW correction was considered by adopting the Grimme's D3 scheme.[4] The constructed Ni SA/CNNS supercell for the free energy calculation contained a 2 × 2 unit cells with 15 Å separations between two layers in the z direction. The free energy of the adsorbed material is calculated based on standard hydrogen electrode（SHE）as proposed by Nørskov et al,[5] and the corresponding formula is as follows：

$$\Delta G=\Delta E+\Delta E_{ZPE}-T\Delta S$$

Where ΔE is the energy calculated by DFT, ΔE_{ZPE} is the correction of zero point energy of adsorbed substance, and $T\Delta S$ is the correction of entropy. VASPKIT is used for the correction of zero point energy and entropy in this paper.[6]

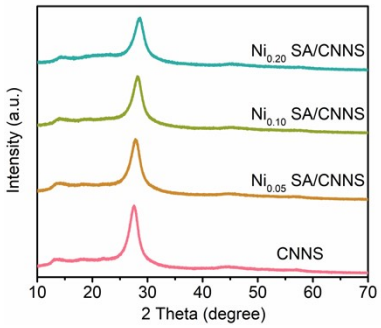

Figure S1. XRD patterns of CNNS, $Ni_{0.05}$ SA/CNNS, $Ni_{0.10}$ SA/CNNS and $Ni_{0.20}$ SA/CNNS.

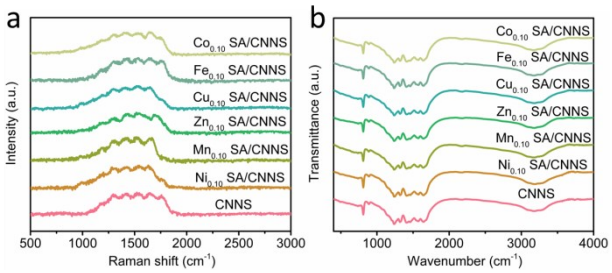

Figure S2. (a) Raman spectra and (b) FT-IR spectrum of CNNS, $Ni_{0.10}$ SA/CNNS and other TM SA/CNNS.

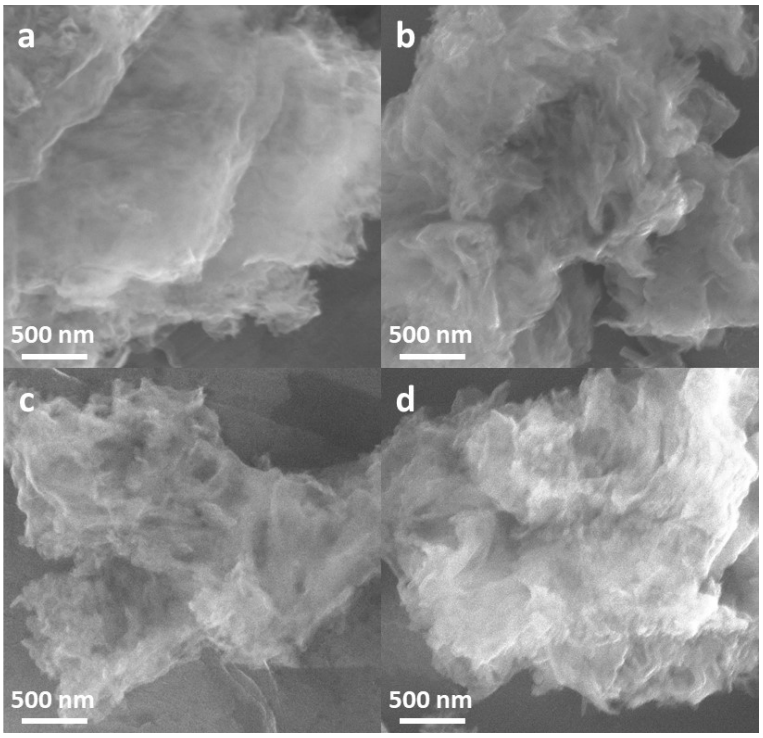

Figure S3. SEM images of (a) CNNS, (b) $Ni_{0.05}$ SA/CNNS, (c) $Ni_{0.10}$ SA/CNNS and (d) $Ni_{0.20}$ SA/CNNS.

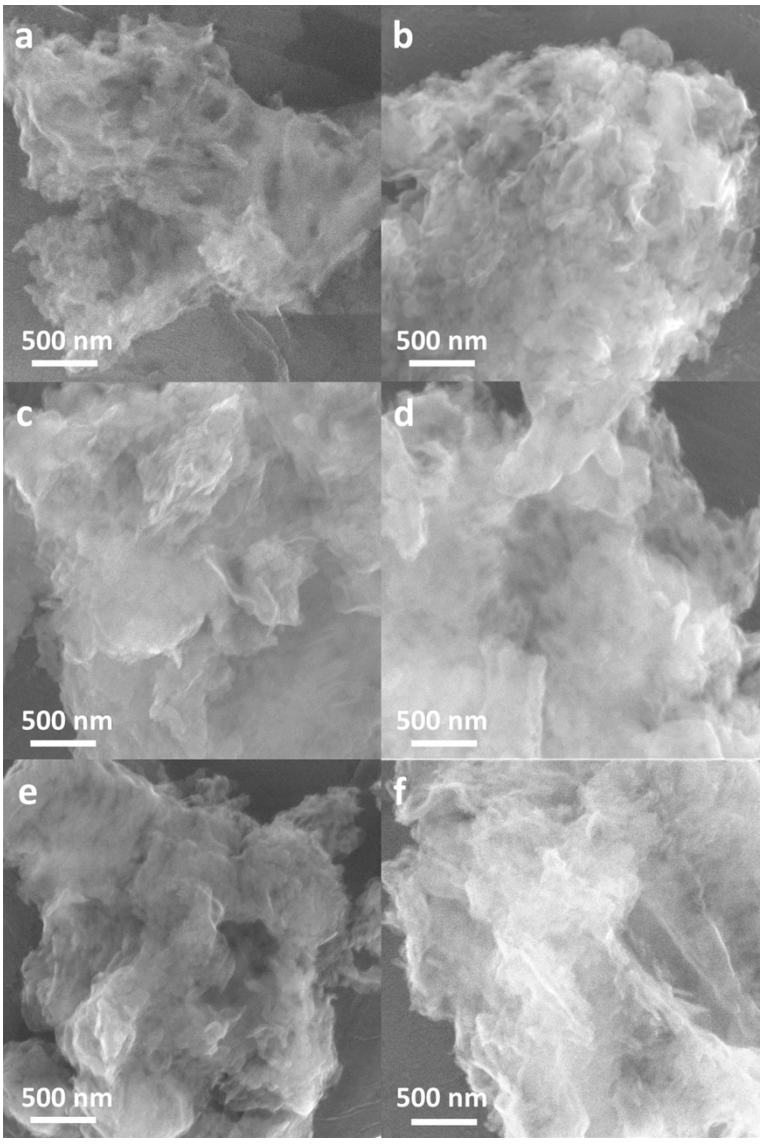

Figure S4. SEM images of (a) $Ni_{0.10}$ SA/CNNS, (b) $Mn_{0.10}$ SA/CNNS, (c) $Zn_{0.10}$ SA/CNNS, (d) $Cu_{0.10}$ SA/CNNS, (e) $Fe_{0.10}$ SA/CNNS and (f) $Co_{0.10}$ SA/CNNS.

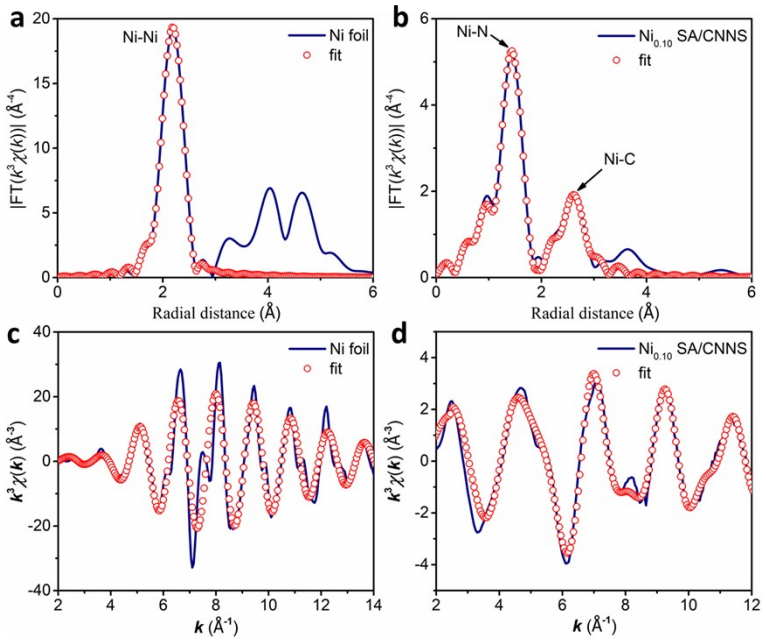

Figure S5. EXAFS R-space fitting curves of (a) Ni foil and (b) $Ni_{0.10}$ SA/CNNS; (b) EXAFS k-space fitting curves of (c) Ni foil and (d) $Ni_{0.10}$ SA/CNNS.

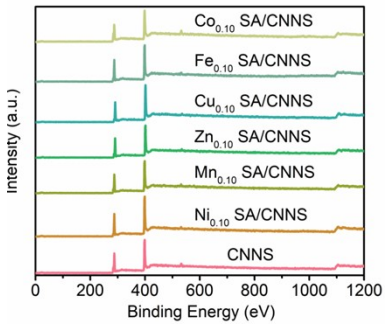

Figure S6. XPS-survey spectra of CNNS, $Ni_{0.10}$ SA/CNNS and other TM SA/CNNS.

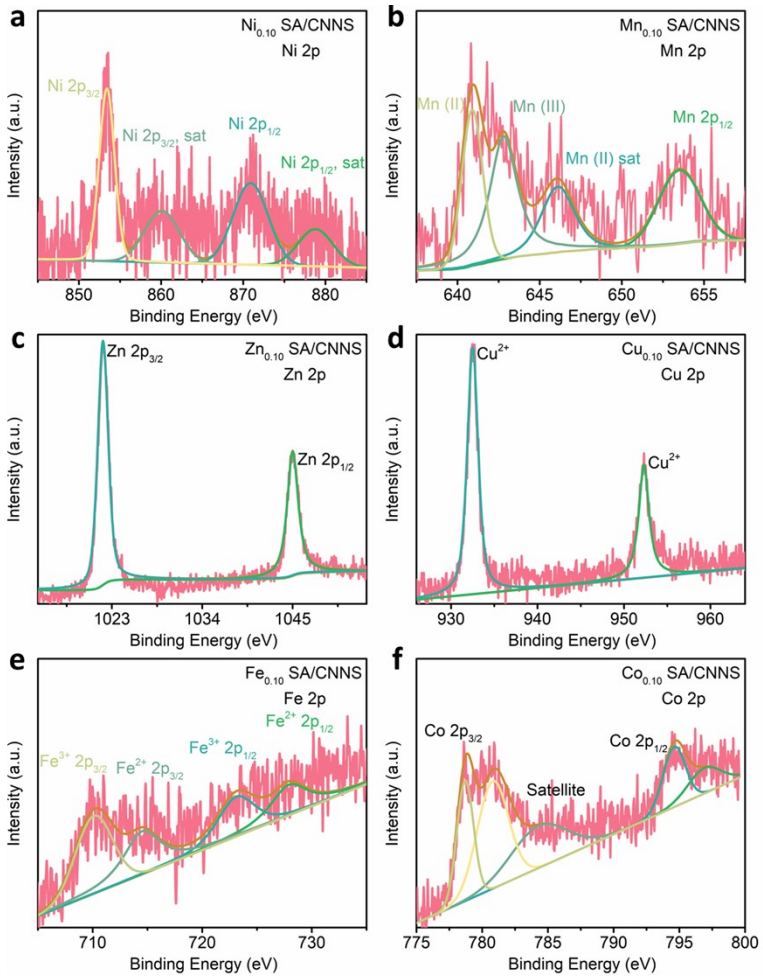

Figure S7. (a) High resolution XPS of Ni 2p spectra of $Ni_{0.10}$ SA/CNNS. (b) High resolution XPS of Mn 2p spectra of $Mn_{0.10}$ SA/CNNS. (c) High resolution XPS of Zn 2p spectra of $Zn_{0.10}$ SA/CNNS. (d) High resolution XPS of Cu 2p spectra of $Cu_{0.10}$ SA/CNNS. (e) High resolution XPS of Fe 2p spectra of $Fe_{0.10}$ SA/CNNS. (f) High resolution XPS of Co 2p spectra of $Co_{0.10}$ SA/CNNS.

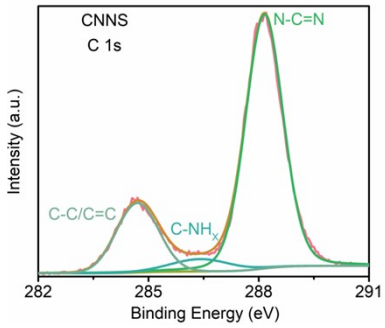

Figure S8. High resolution XPS C 1s spectra of CNNS.

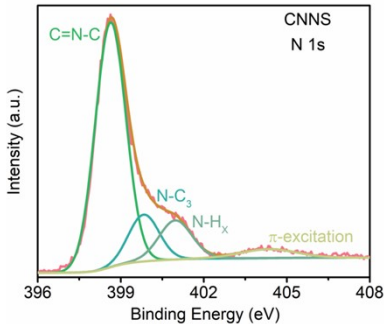

Figure S9. High resolution XPS N 1s spectra of CNNS.

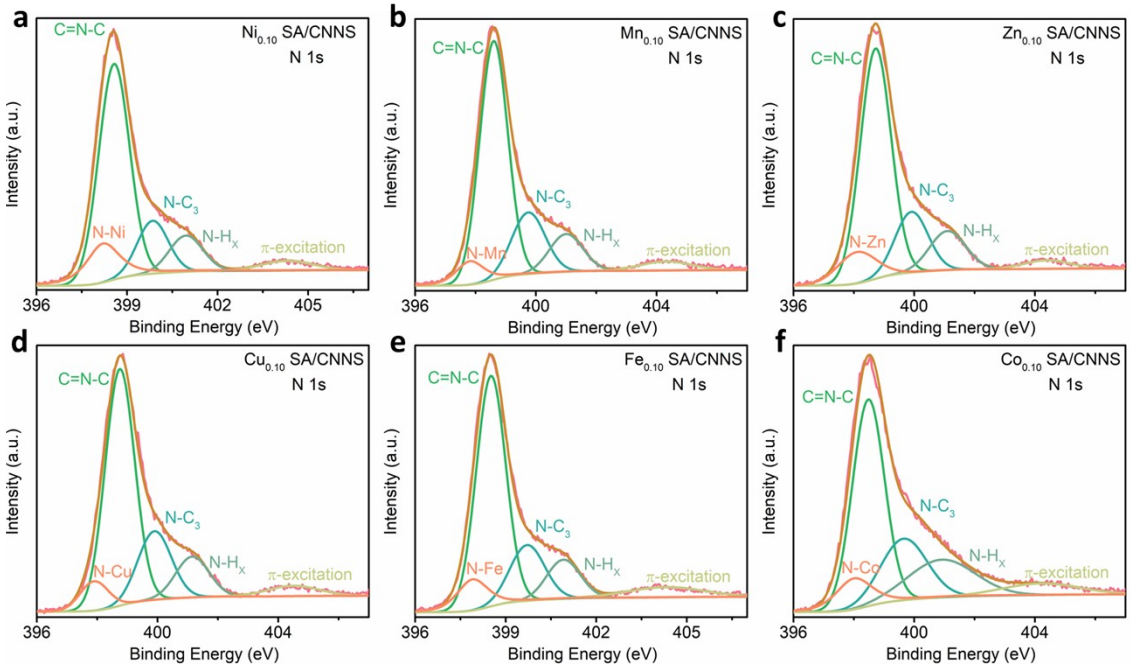

Figure S10. High resolution XPS of N 1s spectra of (a) $Ni_{0.10}$ SA/CNNS, (b) $Mn_{0.10}$ SA/CNNS, (c) $Zn_{0.10}$ SA/CNNS, (d) $Cu_{0.10}$ SA/CNNS, (e) $Fe_{0.10}$ SA/CNNS and (f) $Co_{0.10}$ SA/CNNS.

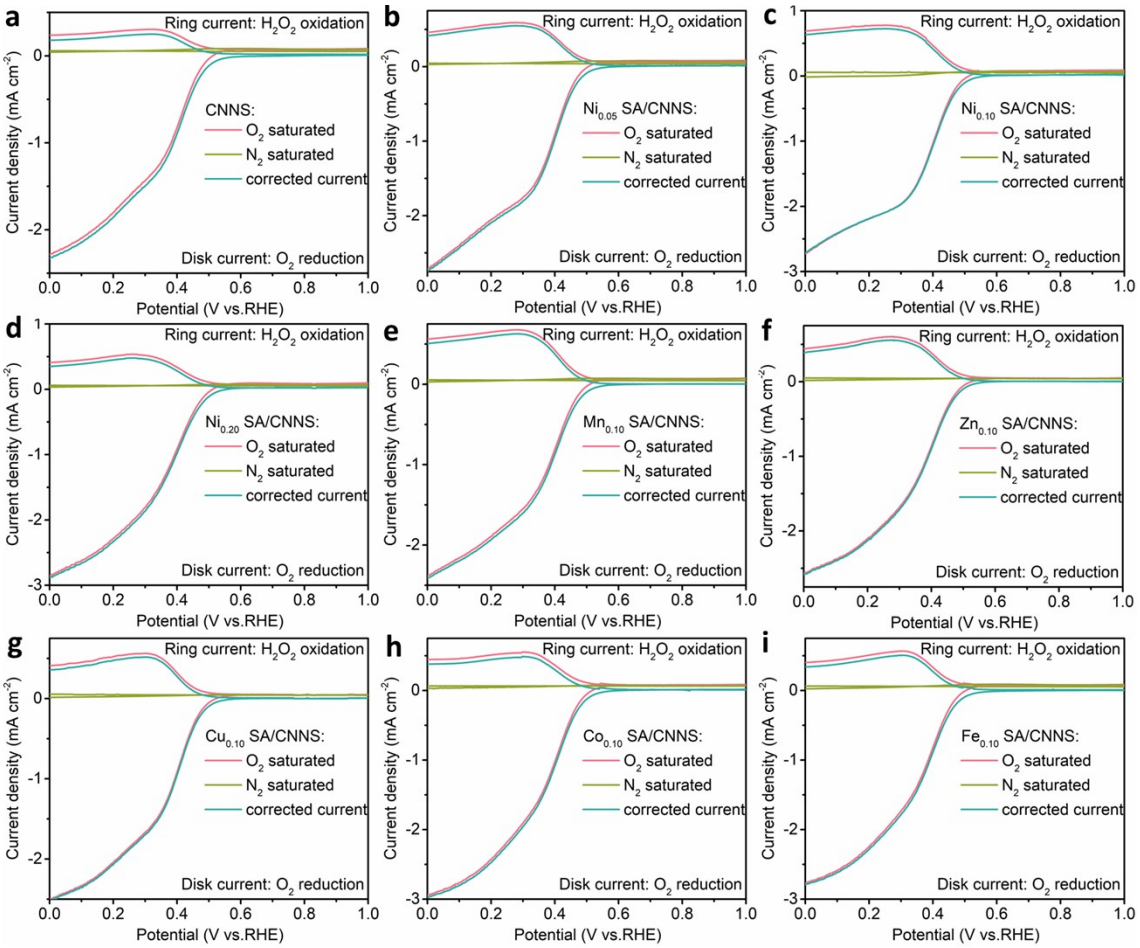

Figure S11. ORR disk current density together with the ring currents for (a) CNNS, (b) $Ni_{0.05}$ SA/CNNS, (c) $Ni_{0.10}$ SA/CNNS, (d) $Ni_{0.20}$ SA/CNNS, (e) $Mn_{0.10}$ SA/CNNS, (f) $Zn_{0.10}$ SA/CNNS, (g) $Cu_{0.10}$ SA/CNNS, (h) $Fe_{0.20}$ SA/CNNS and (i) $Co_{0.20}$ SA/CNNS recorded in O_2-saturated and N_2-saturated 0.1 M PBS. The LSV of ORR is obtained by subtracting the capacitive current in N_2-saturated electrolyte from the O_2-saturated ORR current.

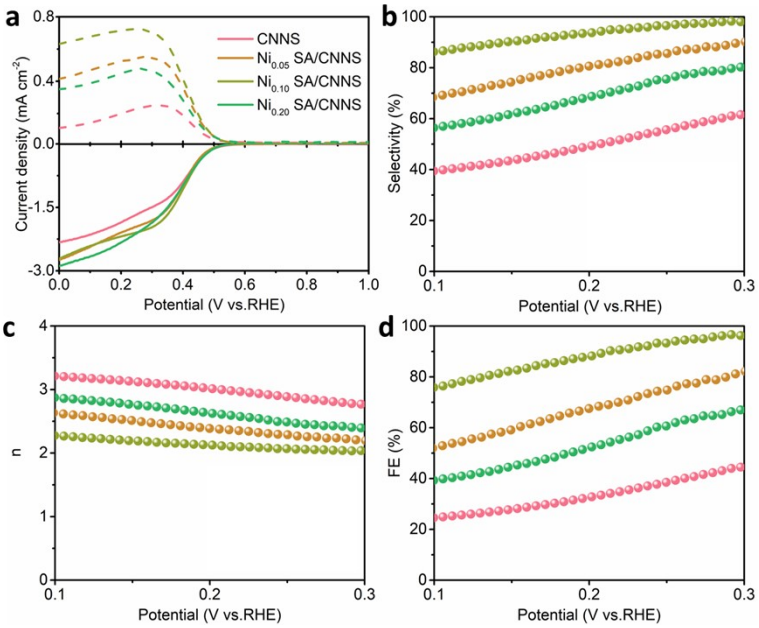

Figure S12. (a) ORR disk current density together with the ring currents at a fixed potential of 1.20 V vs. RHE, (b) H_2O_2 selectivity (H_2O_2 %), (c) the calculated electron transfer number (n) and (d) the faradaic efficiency (FE%) of CNNS, $Ni_{0.05}$ SA/CNNS, $Ni_{0.10}$ SA/CNNS and $Ni_{0.20}$ SA/CNNS in 0.1 M PBS.

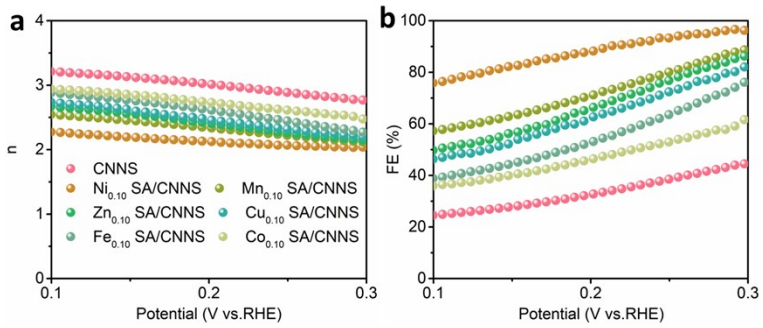

Figure S13. (a) The calculated electron transfer number (n) and (b) the faradaic efficiency (FE%) of CNNS, $Ni_{0.10}$ SA/CNNS and other TM SA/CNNS in 0.1 M PBS.

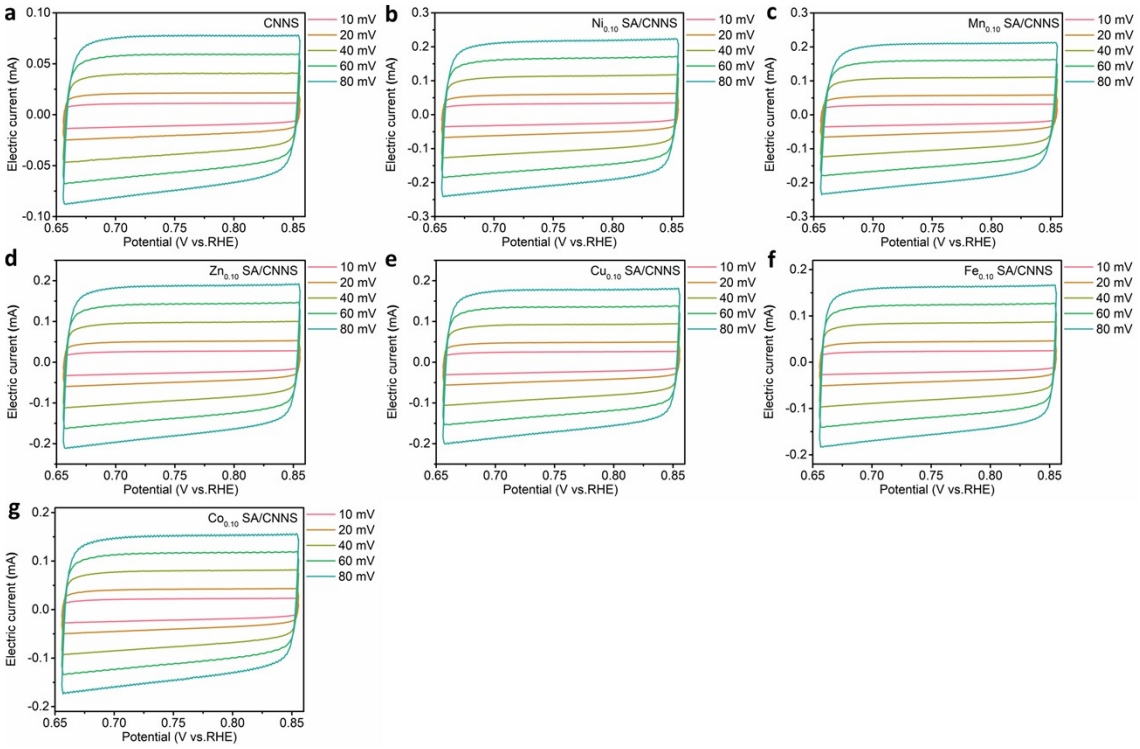

Figure S14. CV curves of (a) CNNS, (b) $Ni_{0.10}$ SA/CNNS, (c) $Mn_{0.10}$ SA/CNNS, (d) $Zn_{0.10}$ SA/CNNS, (e) $Cu_{0.10}$ SA/CNNS, (f) $Fe_{0.10}$ SA/CNNS and (g) $Co_{0.10}$ SA/CNNS measured in 0.1 M PBS at different scan rates (10, 20, 40, 60, and 80 mV s^{-1}).

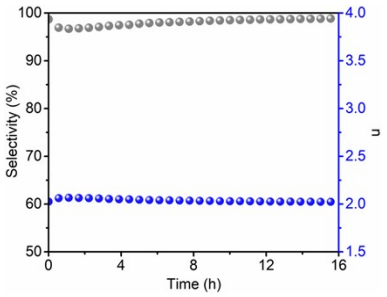

Figure S15. Selectivity and the calculated electron transfer number (n) corresponding to stability measurements of $Ni_{0.10}$ SA/CNNS at a fixed disk potential of 0.3 V vs. RHE.

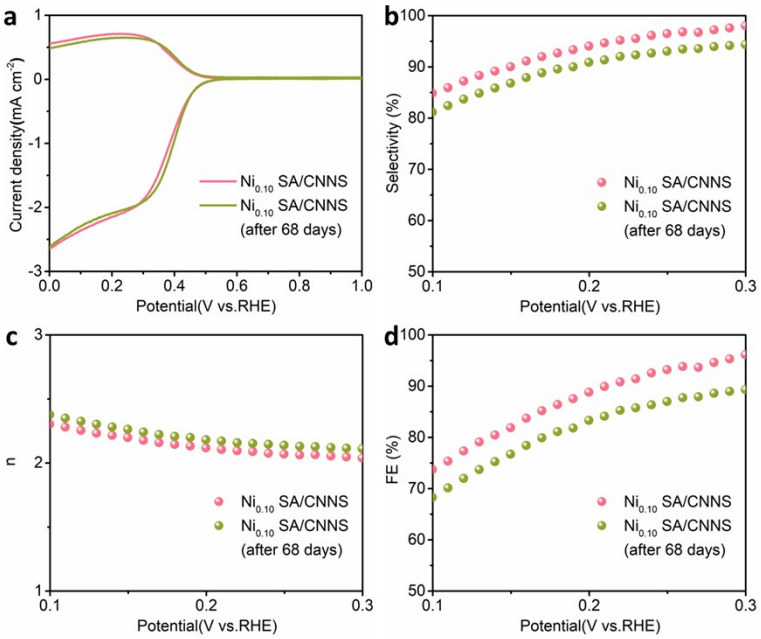

Figure S16. The comparison of (a) current densities, (b) selectivity, (c) the calculated electron transfer number (n) and (d) the faradaic efficiency (FE%) of the same $Ni_{0.10}$ SA/CNNS ink before and after 68 days

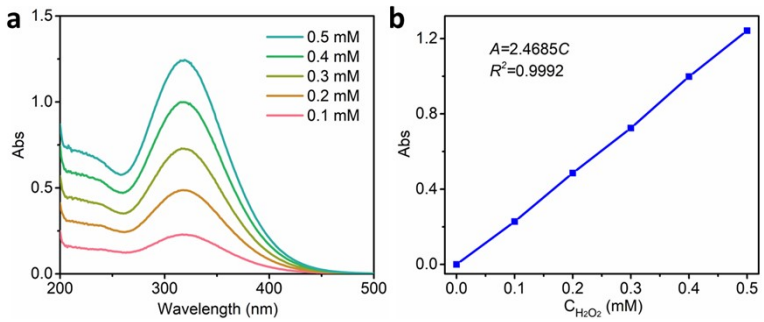

Figure S17. (a) The absorbance value of $Ce(SO_4)_2$ with different concentrations. (b) The linear relationship between the concentration of $Ce(SO_4)_2$ and the absorbance.

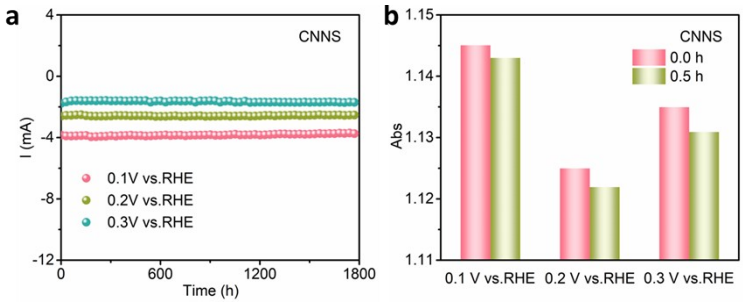

Figure S18. (a) I-t curves of CNNS in O_2-saturted 0.1 M PBS at different potentials. (b) The absorbance value of $Ce(SO_4)_2$ after reacting with H_2O_2 that produced by CNNS at different potentials.

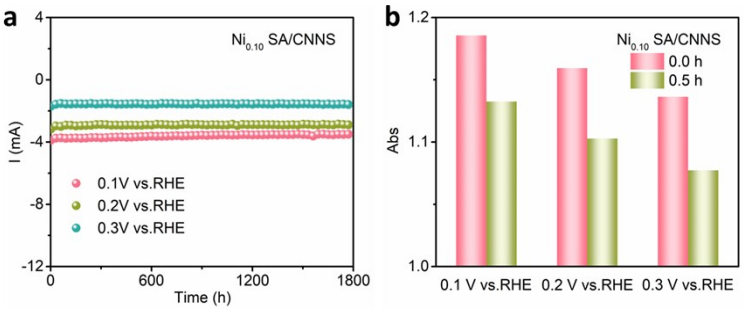

Figure S19. (a) I-t curves of $Ni_{0.10}$ SA/CNNS in O_2-saturted 0.1 M PBS at different potentials. (b) The absorbance value of $Ce(SO_4)_2$ after reacting with H_2O_2 that produced by $Ni_{0.10}$ SA/CNNS at different potentials.

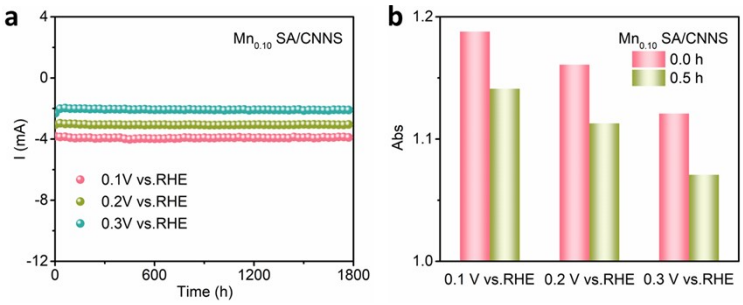

Figure S20. (a) I-t curves of $Mn_{0.10}$ SA/CNNS in O_2-saturted 0.1 M PBS at different potentials. (b) The absorbance value of $Ce(SO_4)_2$ after reacting with H_2O_2 that produced by $Mn_{0.10}$ SA/CNNS at different potentials.

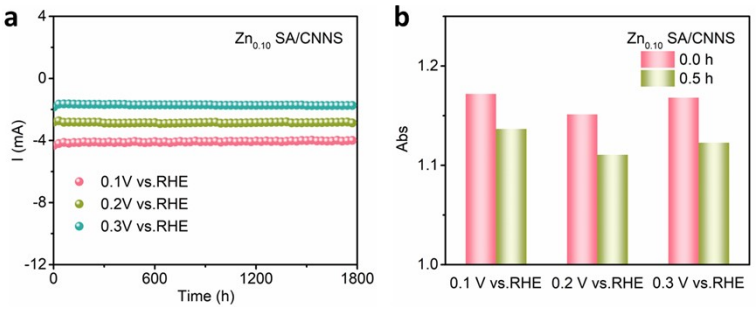

Figure S21. (a) I-t curves of $Zn_{0.10}$ SA/CNNS in O_2-saturted 0.1 M PBS at different potentials. (b) The absorbance value of $Ce(SO_4)_2$ after reacting with H_2O_2 that produced by $Zn_{0.10}$ SA/CNNS at different potentials.

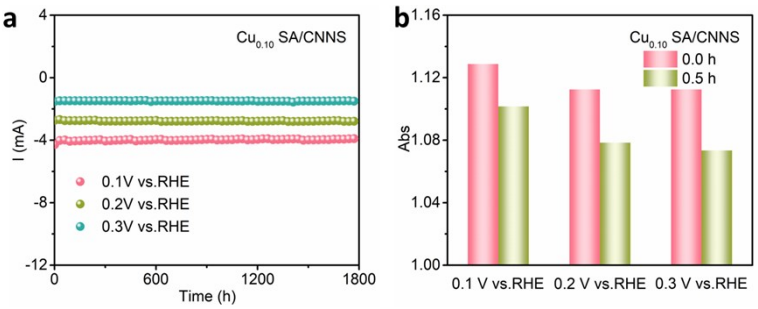

Figure S22. (a) I-t curves of $Cu_{0.10}$ SA/CNNS in O_2-saturted 0.1 M PBS at different potentials. (b) The absorbance value of $Ce(SO_4)_2$ after reacting with H_2O_2 that produced by $Cu_{0.10}$ SA/CNNS at different potentials.

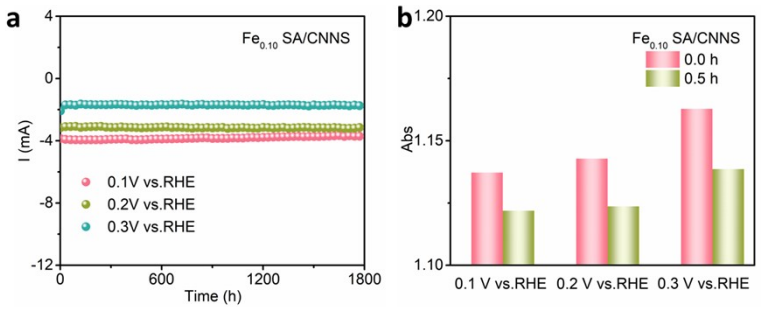

Figure S23. (a) I-t curves of $Fe_{0.10}$ SA/CNNS in O_2-saturted 0.1 M PBS at different potentials. (b) The absorbance value of $Ce(SO_4)_2$ after reacting with H_2O_2 that produced by $Fe_{0.10}$ SA/CNNS at different potentials.

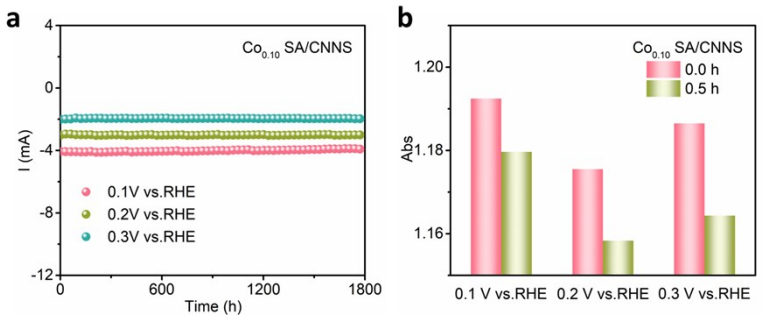

Figure S24. (a) I-t curves of $Co_{0.10}$ SA/CNNS in O_2-saturted 0.1 M PBS at different potentials. (b) The absorbance value of $Ce(SO_4)_2$ after reacting with H_2O_2 that produced by $Co_{0.10}$ SA/CNNS at different potentials.

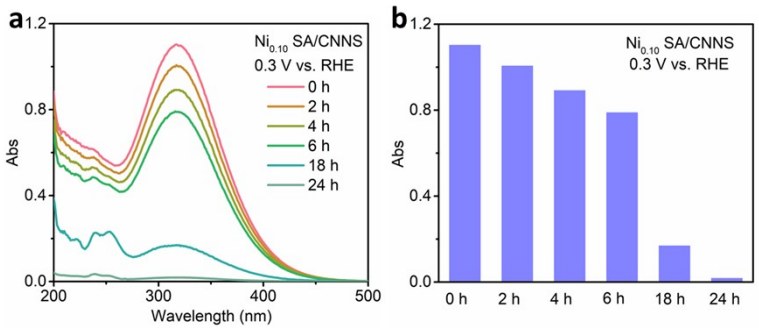

Figure S25. (a) and (b) The absorbance value of $Ce(SO_4)_2$ after reacting with H_2O_2 that produced by $Ni_{0.10}$ SA/CNNS at different times.

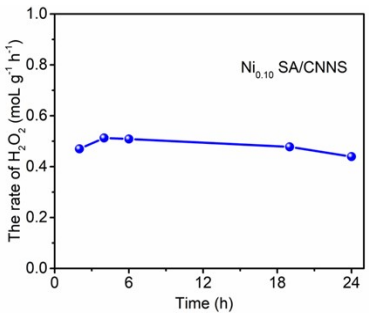

Figure S26. The rate of H_2O_2 of $Ni_{0.10}$ SA/CNNS at different times.

Table S1. The crystallite size of CNNS, $Ni_{0.10}$ SA/CNNS and other TM SA/CNNS, which is calculated by Debye-Scherrer equation based on the XRD patterns.

	2θ (°)	**B_{hkl} (rad)**	**D_{hkl} (nm)**
CNNS	27.34	0.013π	3.45
$Ni_{0.10}$ SA/CNNS	28.34	0.011π	4.10
$Mn_{0.10}$ SA/CNNS	28.12	0.008π	5.88
$Zn_{0.10}$ SA/CNNS	27.83	0.009π	5.27
$Cu_{0.10}$ SA/CNNS	27.83	0.008π	5.91
$Fe_{0.10}$ SA/CNNS	28.15	0.008π	5.44
$Co_{0.10}$ SA/CNNS	28.02	0.009π	4.75

Debye-Scherrer equation: $D_{hkl} = K\lambda/(B_{hkl}\cos\theta)$, where D_{hkl} is the crystallite size in the direction perpendicular to the lattice planes, hkl are the Miller indices of the planes being analysed, K is a numerical factor frequently referred to as the crystallite-shape factor, λ is the wavelength of the X-rays, B_{hkl} is the width (full-width at half-maximum) of the X-ray diffraction peak in radians and θ is the Bragg angle.

Table S2. EXAFS fitting parameters at the Ni k-edge for various samples (S_0^2=0.778).

Sample	Shell	*CN*[a]	*R*(Å)[b]	σ^2(Å^2)[c]	ΔE_0(eV)[d]	*R* factor
Ni foil	Ni-Ni	12*	2.48±0.01	0.0059±0.0002	7.4±0.3	0.0021
Sample Ni	Ni-N	3.2	1.84±0.01	0.0032±0.0010	3.0±1.3	0.0148
	Ni-C	3.4	2.88±0.02	0.0032±0.0028		

[a]*CN*, coordination number; [b]*R*, distance between absorber and backscatter atoms; [c] σ^2, Debye-Waller factor to account for both thermal and structural disorders; [d] ΔE_0, inner potential correction; *R* factor indicates the goodness of the fit. $S0^2$ was fixed to 0.778, according to the experimental EXAFS fit of Ni foil by fixing *CN* as the known crystallographic value. Fitting range: 3.0 ⩽ *k* (/Å) ⩽ 13.8 and 1.5 ⩽ *R* (Å) ⩽ 3.0 (Ni foil); 3.0 ⩽ *k* (/Å) ⩽ 12.5 and 1.0 ⩽ *R* (Å) ⩽ 3.0 (Sample Ni). A reasonable range of EXAFS fitting parameters: 0.700 < S_0^2 < 1.000; *CN* > 0; σ^2 > 0 Å^2; | ΔE_0| < 10 eV; *R* factor < 0.02.

Table S3. The atomic percentages of carbon species (N-C=N, C-O, C-C/C=C) in CN, $Ni_{0.10}$ SA/CNNS, $Mn_{0.10}$ SA/CNNS, $Zn_{0.10}$ SA/CNNS, $Cu_{0.10}$ SA/CNNS, $Fe_{0.10}$ SA/CNNS and $Co_{0.10}$ SA/CNNS.

	Percentage of N-C=N (%)	**Percentage of C-NH_X (%)**	**Percentage of C-C/C=C (%)**
CN	73	6	21
$Ni_{0.10}$ SA/CNNS	92	2	6
$Mn_{0.10}$ SA/CNNS	90	2	8
$Zn_{0.10}$ SA/CNNS	86	5	9
$Cu_{0.10}$ SA/CNNS	85	3	12
$Fe_{0.10}$ SA/CNNS	80	4	16
$Co_{0.10}$ SA/CNNS	67	6	27

Table S4. The comparisons of different electrocatalysts towards $2e^-$ ORR at different pH.

	Catalyst	Electrolyte	Selectivity	Activity (V vs. RHE) @ 0.1 mA cm^{-2}	Stability	Applied potential (V vs. RHE)	H_2O_2 yield rate (mol g_{cat}^{-1} h^{-1})	Ref.
Neutral electrolyte	$Ni_{0.10}$ SA/CNNS	0.1M PBS	98%	~0.55	The H_2O_2 selectivity was maintained in the range of 96.6-98.8% at 16h.	0.3	~0.503	This work
	$Mn_{0.10}$ SA/CNNS	0.1M PBS	95%	~0.57	-	0.3	~0.423	This work
	$Zn_{0.10}$ SA/CNNS	0.1M PBS	93%	~0.56	-	0.3	~0.385	This work
	$Cu_{0.10}$ SA/CNNS	0.1M PBS	90%	~0.56	-	0.3	~0.332	This work
	Pd-Se-B NC	0.1M KPi	85±5%	~0.70	Pd-Se-B NC exhibited the H_2O_2 FE values of > 70% over the entire potential range with the highest FE being 90 ± 3%.	0.55	-	*7*
	MCHS-9:1	0.1M PBS	99%	~0.57	The cyclic voltammograms obtained before and after ADT are very similar, which suggests that our catalyst shows high stability.	0.57	-	*8*
	Co/NC	0.1M PBS	90%	~0.72	The chronoamperometric result shows that the current density remained stable for 10 h without discernible decay. The final concentration of H_2O_2 (20.4 mm) is determined by titration method confirms the FE of 84.2% throughout the entire process.	0.3	-	*9*
	MBC-2	0.1M PBS	87%	~0.32	The i-t curve of the MBC-2 at −0.7 V potential shows unchanged current density	0.4	0.005	*10*

					during 6-h operation, indicating a good electrochemical stability of the catalyst.			
	Co SACs	0.5M NaCl	93.7%	~0.65	The flow cell with the two-electron-transfer ORR pathway at the cathode and CER at the anode shows stable voltage at a current density of 50 mA cm^{-2} for 24 h operation.	0.55	-	*11*
Acidic electrolyte	Co_{SA}-N-CNTS	0.5M H_2SO_4	95%	~0.7	after 5000 continuous cycles of accelerated durability test (ADT), CoSA-N-CNTs catalyst shows scarcely attenuation in comparison with the initial curve, and the half-wave potential shifts negatively of 1 mV only.	0.6	0.974	*12*
	CoNCF-HNO_3	0.5M H_2SO_4	91%	~0.65	-	0.4	-	13
	P-Co@C-800	0.1M $HClO_4$	94%	~0.61	Both the disk and ring current densities change little after 10 h of stability test. The composition and morphology are well maintained, suggesting excellent stability of P-Co@C-700 nanocages.	0.45	57	*14*
	MesoC-Co	0.1M $HClO_4$	80%	~0.73	During the 24 h continuous test, the Faraday efficiency of H_2O_2 synthesis is also maintained at about 80%, corresponding	0.5	0.12	*15*

					to a H_2O_2 selectivity of 88%			
	Mn-O/N@NCs-50	0.1M $HClO_4$	80%	~0.47	-	0.4	-	[16]
	p–Co–N–C	0.5M H_2SO_4	90%	~0.65	-	0.5	2460.8	[17]
	h-Pt_1-CuS_x	0.1M $HClO_4$	96%	~0.65	After 10,000 cyclic voltammetry (CV) cycles between 0.1 and 0.8 V, the declines in H_2O_2 selectivity and current were less than 2%	0.7	546.0	[18]
	NiS_2	0.5M H_2SO_4	99%	~0.56	The NiS_2/CP's current density with minor variation during the 24 000 s of ORR electrolysis also suggests the good long-term stability	0.4	1.25	[19]
Alkaline electrolyte	Ni MOF NSs	0.1 M KOH (pH=13)	~98% (0.6 V_{RHE})	~0.66	2% loss in selectivity after 20,000 cycles of CV testing	0.6	0.08	[20]
	MOF NSs-300	0.1 M KOH (pH=13)	~99% (0.6 V_{RHE})	~0.66	~13% loss in selectivity after 10,000 cycles of CV testing	0.6	6.5	[21]
	Mo SAC	0.1 M KOH (pH=13)	~95% (0.6 V_{RHE})	~0.73	Retain the initial ~95% selectivity after 8-h operation	-	-	[22]
	Ni-SA/G	0.1 M KOH (pH=13)	~94% (0.3 V_{RHE})	~0.68	A decrease of only ~7% after 4000 cycles	-	-	[23]
	Fe-CNT	0.1 M KOH (pH=13)	~95% (0.6 V_{RHE})	~0.77	A stable H_2O_2 selectivity of above 90% over the 8 h continuous operation	-	-	[24]
	Co-CNT	0.1 M KOH (pH=13)	~74.8% (0.6 V_{RHE})	~0.75	-	-	-	[24]
	Pd-CNT	0.1 M KOH (pH=13)	~90% (0.6 V_{RHE})	~0.73	-	-	-	[24]
	PEI50CMK3_800T	0.1 M KOH (pH=13)	~83% (0.3 V_{RHE})	~0.70	Negligible changes in selectivity after 4 h testing	0.3	0.32	[25]
	CMK-3	0.1 M KOH (pH=13)	~82% (0.3 V_{RHE})	~0.70	Excellent stability during the successive	0.1	0.56	[26]

					electrochemical H_2O_2 production within 6 h			
	N-doped graphene	0.1 M KOH (pH=13)	~84% (0.6 V_{RHE})	~0.65	-	0.1	0.21	[27]
	G-COF-T	0.1 M KOH (pH=13)	~75% (0.3 V_{RHE})	~0.60	The H_2O_2 production revealed pseudo first-order kinetics over 2 h electrolysis as depicted by the nearly linear plots of H_2O_2 yield versus time	0.1	1.29	[28]
	O-CNTs	0.1 M KOH (pH=13)	~90% (0.6 V_{RHE})	~0.72	Negligible changes in selectivity after ~10-h testing	-	-	[29]

REFERENCES

1. G. Kresse and J. Furthmüller, *Phys. Rev. B*, 1996, **54**, 11169-11186.
2. J. P. Perdew, K. Burke and M. Ernzerhof, *Physical Review Letters*, 1996, **77**, 3865-3868.
3. P. E. Blöchl, *Phys. Rev. B*, 1994, **50**, 17953-17979.
4. Y.S. Lin, G.D. Li, S.P. Mao and J.D. Chai, *J. Chem. Theory Comput.*, 2013, **9**, 263-272.
5. J. K. Nørskov, J. Rossmeisl, A. Logadottir, L. Lindqvist, J. R. Kitchin, T. Bligaard and H. Jónsson, *J. Phys. Chem. B*, 2004, **108**, 17886-17892.
6. V. Wang, N. Xu, J.C. Liu, G. Tang and W.T. Geng, *Comput. Phys. Commun.*, 2021, **267**, 108033.
7. J. Lee, S. W. Choi, S. Back, H. Jang and Y. J. Sa, *Appl. Catal. B: Environ.*, 2022, **309**, 121265.
8. Y. Pang, K. Wang, H. Xie, Y. Sun, M.M. Titirici and G.L. Chai, *ACS Catal.*, 2020, **10**, 7434-7442.
9. H. Shen, N. Qiu, L. Yang, X. Guo, K. Zhang, T. Thomas, S. Du, Q. Zheng, J. P. Attfield, Y. Zhu and M. Yang, *Small*, 2022, **18**, 2200730.
10. M. Gao, Z.Y. Wang, Y.R. Yuan, W.W. Li, H.Q. Liu and T.Y. Huang, *Chem. Eng. J.*, 2022, **434**, 134788.
11. Q. Zhao, Y. Wang, W.H. Lai, F. Xiao, Y. Lyu, C. Liao and M. Shao, *Energy. Environ. Sci.*, 2021, **14**, 5444-5456.
12. W. Liu, C. Zhang, J. Zhang, X. Huang, M. Song, J. Li, F. He, H. Yang, J. Zhang and D. Wang, *Appl. Catal. B: Environ.*, 2022, **310**, 121312.
13. W. Liu, J. Feng, R. Yin, Y. Ni, D. Zheng, W. Que, X. Niu, X. Dai, W. Shi, F. Wu, J. Yang and X. Cao, *Chem. Eng. J.* 2022, **430**, 132990.
14. Y. Wang, Y. Zhou, Y. Feng and X.Y. Yu, *Adv. Funct. Mater.*, 2022, **32**, 2110734.
15. L. Jing, Q. Tian, P. Su, H. Li, Y. Zheng, C. Tang and J. Liu, *J. Mater. Chem. A*, 2022, **10**, 4068-4075.
16. A. Byeon, J. Cho, J. M. Kim, K. H. Chae, H.Y. Park, S. W. Hong, H. C. Ham, S. W. Lee, K. R. Yoon and J. Y. Kim, *Nanoscale Horiz.*, 2020, **5**, 832-838.
17. J. Zhang, W. Liu, F. He, M. Song, X. Huang, T. Shen, J. Li, C. Zhang, J. Zhang and D. Wang, *Chem. Eng. J.*, 2022, **438**, 135619.
18. R. Shen, W. Chen, Q. Peng, S. Lu, L. Zheng, X. Cao, Y. Wang, W. Zhu, J. Zhang, Z. Zhuang, C. Chen, D. Wang and Y. Li, *Chem*, 2019, **5**, 2099-2110.
19. J. Liang, Y. Wang, Q. Liu, Y. Luo, T. Li, H. Zhao, S. Lu, F. Zhang, A. M. Asiri, F. Liu, D. Ma and X. Sun, *J. Mater. Chem. A*, 2021, **9**, 6117-6122.
20. M. Wang, X. Dong, Z. Meng, Z. Hu, Y.G. Lin, C.K. Peng, H. Wang, C.W. Pao, S. Ding, Y. Li, Q. Shao and X. Huang, *Angew. Chem. Int. Ed.*, 2021, **60**, 11190-11195.
21. M. Wang, N. Zhang, Y. Feng, Z. Hu, Q. Shao and X. Huang, *Angew. Chem. Int. Ed.*, 2020, **59**, 14373-14377.
22. C. Tang, Y. Jiao, B. Shi, J.N. Liu, Z. Xie, X. Chen, Q. Zhang and S.Z. Qiao, *Angew. Chem. Int. Ed.*, 2020, **59**, 9171-9176.
23. X. Song, N. Li, H. Zhang, L. Wang, Y. Yan, H. Wang, L. Wang and Z. Bian, *ACS Appl. Mater. Int.*, 2020, **12**, 17519-17527.
24. K. Jiang, S. Back, A. J. Akey, C. Xia, Y. Hu, W. Liang, D. Schaak, E. Stavitski, J. K. Nørskov, S. Siahrostami and H. Wang, *Nat. Commun.*, 2019, **10**, 3997.

25. Y. Sun, S. Li, Z. P. Jovanov, D. Bernsmeier, H. Wang, B. Paul, X. Wang, S. Kühl and P. Strasser, *ChemSusChem*, 2018, **11**, 3388-3395.
26. Y. Sun, I. Sinev, W. Ju, A. Bergmann, S. Dresp, S. Kühl, C. Spöri, H. Schmies, H. Wang, D. Bernsmeier, B. Paul, R. Schmack, R. Kraehnert, B. Roldan Cuenya and P. Strasser, *ACS Catal.*, 2018, **8**, 2844-2856.
27. L. Han, Y. Sun, S. Li, C. Cheng, C. E. Halbig, P. Feicht, J. L. Hübner, P. Strasser and S. Eigler, *ACS Catal.*, 2019, **9**, 1283-1288.
28. J. Zhang, G. Zhang, S. Jin, Y. Zhou, Q. Ji, H. Lan, H. Liu and J. Qu, *Carbon*, 2020, **163**, 154-161.
29. Z. Lu, G. Chen, S. Siahrostami, Z. Chen, K. Liu, J. Xie, L. Liao, T. Wu, D. Lin, Y. Liu, T. F. Jaramillo, J. K. Nørskov and Y. Cui, *Nat. Catal.*, 2018, **1**, 156-162.